Nuclear Science and Techniques (2026) 37:79
https://doi.org/10.1007/s41365-026-01908-3

Production of ^{99}Mo via photofission reaction in natural-uranium-bearing molten salt targets

Jun-Ze Lin[1,2,3] · Bo-Lin Fu[1,2,3] · De-Yang Cui[1,3] · Xiao-Xiao Li[1,2,3] · Cheng-Gang Yu[1,2,3] · Jian-Hui Wu[1,2,3] · Jin-Gen Chen[1,2,3] · Xiang-Zhou Cai[1,2,3]

Received: 31 July 2025 / Revised: 10 September 2025 / Accepted: 11 October 2025 / Published online: 9 February 2026

Abstract

This study proposes a method for ^{99}Mo production via electron accelerator irradiation of a natural–uranium–bearing liquid molten salt target, with advantages including low nuclear proliferation risk, online extraction capability, and low construction costs. The approach primarily produces ^{99}Mo through photofission of uranium (~95%), specifically ^{238}U(γ,f). Secondary neutrons, originating from photonuclear interactions or fission processes, contribute minimally (~5%) to ^{99}Mo production owing to their high energies and low fission cross sections. Key parameter analyses revealed that fluoride salt systems exhibit higher ^{99}Mo yield. Their performance stems from high bremsstrahlung energy loss rate and superior photon yield, making them optimal molten salt target materials. To maximize photofission and photoneutron cross sections while minimizing high-energy gamma ray shielding requirements, an electron beam energy range of 40–80 MeV is recommended. To suppress local hot spots and prevent molten salt boiling, flow conditions were introduced to enhance convective heat transfer, effectively reducing the peak temperature. At a flow velocity of 0.5 m/s and under 80 MeV energy conditions, the maximum system temperature is only 808.9 K, which is significantly lower than the boiling point of 1773 K. Under optimized parameters, the maximum annual production capacity of ^{99}Mo reaches 4486.49 Ci, sufficient for millions of diagnostic procedures and equivalent to 16.37% of China's projected demand for 2030. This method provides a viable pathway for stable, large-scale ^{99}Mo production.

Keywords ^{99}Mo · Electron accelerator · Molten salt · Natural uranium · Photofission

1 Introduction

As a pivotal medical radioisotope, Technetium-99m (^{99m}Tc) is extensively utilized in clinical diagnostics [1, 2], accounting for approximately 80% of global nuclear medicine radioisotope consumption [3]. ^{99m}Tc is primarily derived from the β^- decay of molybdenum–99 (^{99}Mo, $T_{1/2} \approx 65.92$ h). Consequently, the stability of the ^{99}Mo supply directly determines the market availability of ^{99m}Tc. According to estimates by the Organization for Economic Cooperation and Development/Nuclear Energy Agency (OECD/NEA), the global demand for ^{99}Mo reached 5.5×10^5 Ci in 2020 and is growing at over 10% annually, attaining 8.8×10^5 Ci by 2030 [4]. Furthermore, according to the "Medium-to-Long-Term Development Plan for Medical Isotopes (2021–2035)", China's annual demand for ^{99}Mo has exceeded 1.6×10^4 Ci since 2019, with a steady 5% annual growth rate.

This work was supported by the National Natural Science Foundation of China (Nos. 12435012, 12175300, and 12475185), Shanghai Natural Science Foundation (No. 24ZR1478500), and Nuclear energy development project (HNKF202210 (24)).

✉ Xiao-Xiao Li
lixiaoxiao@sinap.ac.cn

✉ Jin-Gen Chen
chenjingen@sinap.ac.cn

[1] Shanghai Institute of Applied Physics, Chinese Academy of Sciences, Shanghai 201800, China

[2] University of Chinese Academy of Sciences, Beijing 100049, China

[3] State Key Laboratory of Thorium Energy, Shanghai Institute of Applied Physics, Chinese Academy of Sciences, Shanghai 201800, China

Currently, the global supply of medical ^{99}Mo is predominantly produced using research reactors in Europe, Canada, Australia, and South Africa, etc. [5, 6]. Owing to the significant nuclear proliferation risks associated with the use of highly enriched uranium (HEU, ^{235}U enrichment >90%), its application is restricted [7, 8]. Therefore, most research reactors have now transitioned to irradiating low enriched uranium (LEU, ^{235}U enrichment <20%) [9]. Most research reactors have exceeded 40 years of operating time and will face shutdown and decommissioning over the next decade [2, 10], potentially triggering a severe "^{99}Mo shortage crisis" that would critically impact ^{99}Mo-importing nations. To sustain the supply of ^{99}Mo, the High Flux Reactor (HFR) in Petten, Netherlands, originally scheduled for shutdown in 2022, had its closure delayed [11]. However, in 2024, due to pipeline deformation above the reactor vessel, it failed to restart as planned after a routine maintenance shutdown, once again causing issues in the global ^{99}Mo supply chain [12]. Meanwhile, Belgium's BR2 reactor and South Africa's Safari-1 reactor are extending their operational cycles to address the shortage [13, 14].

The international community is committed to developing new sustainable ^{99}Mo production methods. In 1992, Chopela and Ball [15, 16] from Babcock & Wilcox (B&W) proposed a Medical Isotope Production Reactor (MIPR). Although this technology has attained commercial viability with small-scale industrial implementation [17–20], MIPR face significant power fluctuations during operation owing to void, chemical, and temperature effects, risking control instabilities [21].

Molten salt reactors (MSRs) use molten salt mixtures as both fuel and primary coolant, offering significant advantages for isotope production, such as high production efficiency and online extraction capabilities [22, 23]. Consequently, global research efforts have increasingly focused on MSR-based ^{99}Mo production with online extraction systems. Studies have confirmed the technical feasibility and promise of MSRs for isotope generation [24, 25], revealing unique behaviors of fission products (e.g., Mo): these products spontaneously migrate from molten salt phase into gas phase, with at least 50% of Mo fragments accumulating in the aerosol phase above the salt surface [26, 27]. This behavior forms the foundation for ^{99}Mo production in MSRs, leading to further evaluations of online ^{99}Mo extraction feasibility from MSRs [22, 28]. Nevertheless, MSR-based isotope production remains predominantly in the theoretical validation and exploratory stages, with critical scientific and technical challenges requiring resolution.

In 2009, the OECD/NEA convened a meeting in Paris to address global ^{99}Mo/^{99m}Tc supply security, establishing the High-Level Group on Medical Isotopes to ensure sustainable global access to these isotopes [6]. Among the various technological approaches, accelerator-based production routes, which either generate ^{99}Mo or directly yield ^{99m}Tc, are recognized as viable medium-to-long-term alternatives owing to their regulatory flexibility, non-proliferation benefits, and low infrastructure/operating costs [29].

Accelerator-based production of ^{99}Mo/^{99m}Tc primarily employs two approaches: direct irradiation of production targets with primary particles (e.g., protons, electrons, deuterons, α-particles) or irradiation of converter targets to generate secondary particles (neutrons/photons) for bombarding production targets. Viable pathways include: ^{100}Mo(γ,n)^{99}Mo, ^{100}Mo(p,2n)^{99m}Tc, ^{100}Mo(p,pn)^{99}Mo, ^{96}Zr(α,n)^{99}Mo, ^{98}Mo(n,γ)^{99}Mo, ^{100}Mo(n,2n)^{99}Mo, ^{235}U(n,f)^{99}Mo, U/Th(p,f)^{99}Mo and ^{238}U(γ,f)^{99}Mo, among others [2, 9, 30–32]. Figure 1 summarizes these accelerator-based production technologies [6].

Proton beam irradiation of natural uranium or thorium-232 (^{232}Th) can produce ^{99}Mo via a (p,f) reaction;

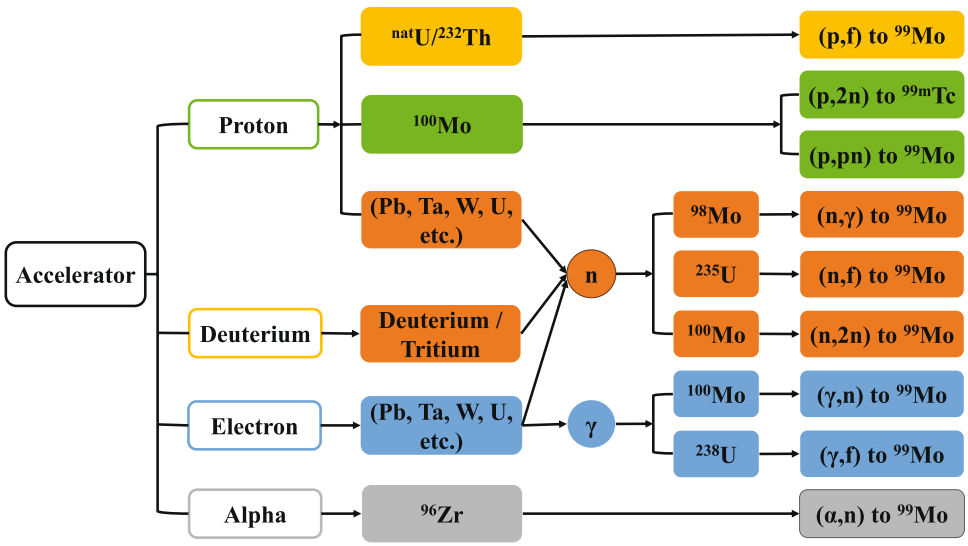

Fig. 1 (Color online) Accelerator–based production technologies for ^{99}Mo/^{99m}Tc

however, the reaction cross sections are low [2]. Alternatively, proton irradiation of ^{100}Mo generates ^{99m}Tc directly through (p,2n) reaction or produces ^{99}Mo via (p,pn) reaction. This approach achieves high ^{99m}Tc yields with lower proton energy requirements ($E_p < 30$ MeV). However, the short half-life of ^{99m}Tc ($T_{1/2} \approx 6.01$ h) restricts long-distance transportation, thus it can only be supplied to surrounding areas. Notably, the competing reaction ^{100}Mo(p,2n)^{99g}Tc produces significant quantities of ^{99g}Tc, compromising radiopharmaceutical purity and imaging efficacy [33, 34]. Secondary particle methods utilize protons or electrons hitting converter targets to generate neutrons/photons, which then irradiate ^{100}Mo or ^{98}Mo to produce ^{99}Mo. Nevertheless, molybdenum-based production routes (involving enriched ^{100}Mo, ^{98}Mo, or natural molybdenum targets) face three critical challenges: (a) low specific activity (0.35–15 Ci/g) owing to the molybdenum carrier component, requiring complex separation processes—significantly below clinical generator requirements (20–500 Ci/g) [35, 36]; (b) prohibitive target costs owing to low yields from natural molybdenum, requiring enriched targets (^{98}Mo or ^{100}Mo at 500–1500 USD/g) [29, 37]; (c) minuscule utilization efficiency (only 0.001% to 0.0001% of Mo atoms are transformed), mandating costly recovery systems and increasing operational expenditures [29, 35, 37, 38].

Building on the MIPR concept, the United States proposed an accelerator-driven subcritical solution reactor for isotope production [39, 40]. However, this method requires high-intensity, long-term stable accelerator neutron sources, posing significant challenges, such as considerable R&D complexity, prohibitively expensive accelerator infrastructure, and high neutron production costs. In 2021, Han et al. [40, 41] proposed an accelerator-based deuterium-tritium (D-T) neutron source subcritical system for producing ^{99}Mo. However, this method requires the use of tritium, which is not only costly but also presents challenges in obtaining possession and operation licenses for tritium. Consequently, Han et al. [9] introduced a novel design for ^{99}Mo production based on a LUE subcritical blanket system (SBS). This system is driven by a Gas Dynamic Trap-based Fusion Neutron Source (GDT–FNS) and utilizes neutrons from the deuterium-deuterium (D-D) fusion reaction to induce the fission of ^{235}U. Alternatively, ^{99}Mo can be produced by α-particle irradiation of ^{96}Zr via (α,n) reaction. To increase the yields, enriched ^{96}Zr targets must be employed, further increasing the production expenses [42].

Ruth [43] proposed photofission of ^{238}U targets using electron accelerators for ^{99}Mo production, emphasizing that while ^{99}Mo yield via ^{238}U(γ,f) reaction is significantly lower than ^{235}U(n,f) production, this is outweighed by the advantage of using safer materials. Naik et al. [44] also validated ^{238}U(γ,f) as a viable ^{99}Mo production route. Concurrently, Naik [45], Thierens [46], and Schmitt [47] measured cumulative ^{99}Mo fission yields from ^{238}U at bremsstrahlung energies of 10 MeV, 25 MeV, and 48 MeV as 4.835%, 6.480%, and 6.600%, respectively. The cumulative yield of ^{99}Mo increases with the incident electron energy. In contrast, fast–neutron–induced fission of ^{238}U achieves a ^{99}Mo cumulative yield of 6.168% [48], demonstrating the comparable efficiencies between photofission and fast-neutron-induced fission. Collectively, these studies establish the technical viability of ^{99}Mo production via ^{238}U(γ,f) reaction. With its inherently high ^{238}U abundance (99.27%), natural uranium emerges as a strategically advantageous target material. The adoption of natural uranium eliminates the enrichment requirements for ^{238}U, substantially reduces target fabrication costs, and minimizes proliferation risks. Naik et al. [44] irradiated a 1 g natural uranium target for 24 h with bremsstrahlung photons generated from a 10 MeV, 4 kW electron beam (10 Hz repetition rate) on a tantalum foil, achieving ^{99}Mo production of (0.309±0.050) mCi-confirming natural uranium's practical utility.

Current accelerator-based ^{99}Mo production predominantly employs solid targets, facing persistent challenges such as complex fabrication, cutting, and dissolution processes, high costs, inability for online extraction, and inadequate heat dissipation. To overcome these limitations, this study integrates the synergistic advantages of liquid molten salts and electron accelerators to propose a method for ^{99}Mo production via electron beam irradiation of natural-uranium-bearing molten salt targets. This approach utilizes the ^{238}U(γ,f) reaction to produce ^{99}Mo, offering significant advantages such as the elimination of HEU, significantly reducing proliferation risks; avoidance of solid-target processing through fluid targets; online extraction and simplified reprocessing, yielding high specific activity of ^{99}Mo; continuous irradiation capability to enhance uranium utilization efficiency; direct irradiation without converter targets, reducing costs and structural complexity; inherent flow–based cooling, reducing cooling requirements and enabling higher beam intensities for increased yields; and lower target fabrication costs with economical molten salts.

A distinctive feature of molten salt targets, compared to solid targets, is their fluidity. This characteristic also introduces numerous new challenges for target system design, including target size and structural design, molten salt circulation system, thermal management and temperature control, as well as material corrosion and compatibility. To evaluate the feasibility of this approach, this study employs Monte Carlo methods to systematically simulate and analyze the critical operational parameters of the ^{99}Mo production system, including molten salt composition, target geometry, incident electron beam energy, temperature distribution, and online extraction efficiency. Based on the parameter analysis, the theoretical annual production capacity of ^{99}Mo was quantitatively projected and comparatively assessed against

China's demand. These findings will provide essential references for the engineering implementation of this production methodology.

2 Materials and methods

2.1 Monte Carlo model

FLUKA has been validated as a reliable tool for modeling radioisotope production [49–51]. Consequently, this study utilized FLUKA to simulate and analyze ^{99}Mo generation via electron irradiation of molten salts. Complementarily, coupled electron-photon transport and bremsstrahlung analyses were conducted using pyPENELOPE [52]. The temperature distribution of the molten salt was analyzed using ANSYS Fluent software [53].

A schematic of ^{99}Mo production via electron beam irradiation of a molten salt target is shown in Fig. 2, comprising two core components: an electron beam and a molten salt target assembly. The electron beam features a radius of 1 cm, an energy range of 20–160 MeV, and an intensity of 1 mA, incident along the positive *Z*-axis. The molten salt target assembly comprises two concentric layers: an inner molten salt layer and an outer cladding layer. The internal cavity was filled with molten salt (Fig. 2b), while the outermost cladding is a 0.5 cm thick nickel-based alloy. Furthermore, to conduct thermal analysis of the molten salt target, the model incorporates the flow process of the molten salt. Accordingly, the inlets and outlets for the molten salt were configured (Fig. 2c). Along the *Y*-axis, the molten salt enters from the bottom and exits from the top of the receiver.

2.2 Reaction models and cross sections

Under electron beam irradiation, the incident electrons initially generate bremsstrahlung photons through interactions with the constituent atoms of the molten salt target. These photons subsequently induce direct (γ,f) reactions with uranium to produce ^{99}Mo or alternatively undergo photonuclear reactions (γ,xn) to generate secondary neutrons. The latter initiates (n,f) reactions on uranium atoms, thereby yielding

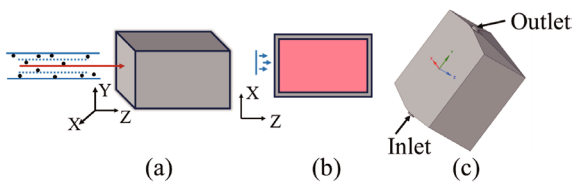

Fig. 2 (Color online) Schematic of ^{99}Mo production via electron irradiated molten salt target: **a** three-dimensional target, **b** *XZ*-section, and **c** three-dimensional target (with inlet and outlet)

additional ^{99}Mo. This reaction cascade is illustrated schematically in Fig. 3. Consequently, ^{99}Mo in molten salt primarily originates from fission of both ^{235}U and ^{238}U, encompassing: direct fission products and decay of short-lived precursor nuclei. Direct fission pathways include both photofission and neutron-induced fission of ^{235}U and ^{238}U, with key precursors nuclei ^{99}Nb ($T_{1/2}$ = 15.0 s) and ^{99m}Nb ($T_{1/2}$ = 2.5 min). Given that their half-lives are negligible compared to ^{99}Mo, fission-generated precursors are assumed to completely decay to ^{99}Mo during irradiation.

Figure 4 displays the (γ,f) reaction cross sections for ^{235}U and ^{238}U extracted from the ENDF/B-VIII.1 database [54]. Within the 10–20 MeV photon energy range, both ^{235}U and ^{238}U exhibit significant (γ,f) cross sections. ^{235}U peaks at 0.33 b (E_γ = 14 MeV), and ^{238}U peaks at 0.16 b (E_γ = 14.5 MeV), indicating feasibility with relatively low electron/photon energies. Neutron-induced fission also contributes to ^{99}Mo production, where secondary neutrons are

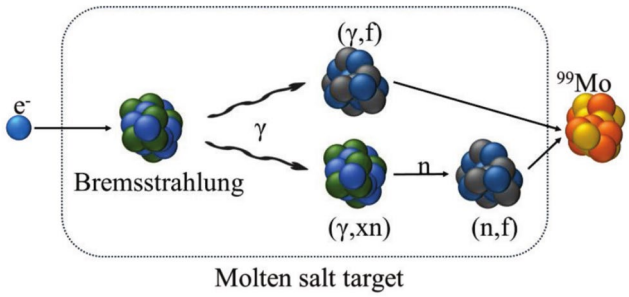

Fig. 3 (Color online) Schematic of the physical process for ^{99}Mo production via electron irradiated molten salt

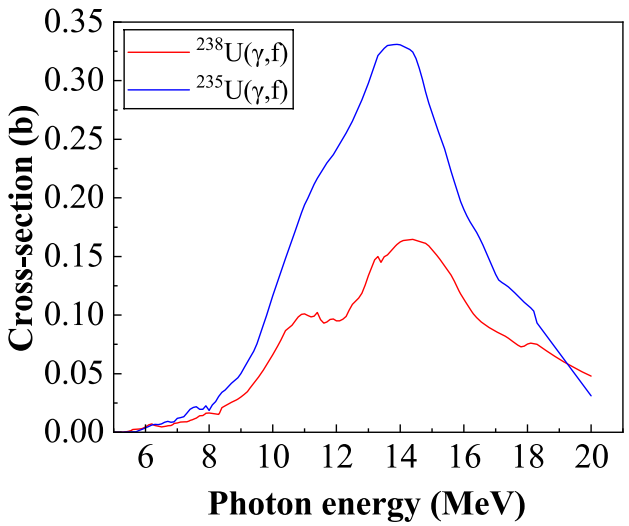

Fig. 4 (Color online) (γ,f) reaction cross sections for ^{235}U and ^{238}U

predominantly generated via photonuclear reactions. Figure 5 illustrates the (γ,xn) cross sections for ^{235}U and ^{238}U, both peaking within 10–20 MeV (^{238}U: 0.73 b at 14 MeV; ^{235}U: 0.52 b at 14.5 MeV). The comparable photofission and photonuclear reaction cross sections between ^{235}U and ^{238}U demonstrate low ^{235}U enrichment requirements, enabling the use of natural uranium.

2.3 Computational methods for online extraction

^{99}Mo predominantly exists in molten salt as ionic species, noble metallic states, and fluoride compounds [22, 55]. The noble metallic state ^{99}Mo adheres to the liquid–gas interfaces of bubbles, enabling online extraction via bubble methods. For instance, in molten salt reactors, helium is injected into the molten salt, circulates, and returns to the pump bowl. Helium exists as dissolved atoms and bubbles. ^{99}Mo enters helium bubbles, adheres to liquid–gas interfaces, and flows to the pump bowl. High-velocity jet spraying within the pump bowl produces a salt mist, that migrates to the degassing module. The off-gas undergoes sequential physical-chemical processes (collection, cooling, separation, adsorption, filtration, purification, and isotopic separation) to produce radiopharmaceutical-grade ^{99}Mo [22].

The ^{99}Mo production method via electron irradiation of molten salt, as proposed in this study, leverages the liquid properties and bubble-based online extraction, thereby simplifying production the processes and reducing costs. However, the physical behavior of ^{99}Mo in molten salts, including ionic-to-metallic transition kinetics, governing constraints, and conversion ratios, remains incompletely understood [22]. Thus, the calculations assume that all ^{99}Mo exists in noble metallic states. Online extraction is modeled using pseudo-decay kinetics with a pseudo-decay factor λ_i. For radionuclide i with inventory N_i and extraction efficiency P (s^{-1}), the differential extracted quantity dN_i within an infinitesimal time is expressed as:

$$\mathrm{d}N_i = N_i P \mathrm{d}t. \tag{1}$$

Therefore, the pseudo-decay factor is expressed as follows:

$$\lambda_i = P. \tag{2}$$

Throughout the irradiation period, the ^{99}Mo production rate is assumed to be constant at Y (Bq/s). Consequently, the temporal evolution of ^{99}Mo activity without online extraction is described as

$$\frac{\mathrm{d}A}{\mathrm{d}t} = Y - \lambda A(t),\ A(0) = 0, \tag{3}$$

where λ denotes the decay constant of ^{99}Mo (s^{-1}), and $A(t)$ represents the activity (Bq) at time t. Integration gives:

$$A(t) = \frac{Y}{\lambda}\left(1 - e^{-\lambda t}\right). \tag{4}$$

From the above equation, as t approaches infinity:

$$A_{\max} = \frac{Y}{\lambda}, \tag{5}$$

$A_{\max}$ denotes the saturation activity, where production and decay reach equilibrium, and ^{99}Mo activity stabilizes. Thus,

$$Y = \lambda A_{\max}. \tag{6}$$

When the extraction efficiency P is introduced, the rate of change of activity $A(t)$ is governed by three components: irradiation production rate Y, radioactive decay rate $\lambda A(t)$, and pseudo-decay rate (extraction efficiency) $\lambda_i A(t)$.

$$\begin{aligned} \frac{\mathrm{d}A}{\mathrm{d}t} &= Y - (\lambda + \lambda_i)A(t) \\ &= Y - (\lambda + P)A(t) \\ A(0) &= 0. \end{aligned} \tag{7}$$

Therefore, integration yields the activity function:

$$A(t) = \frac{Y}{\lambda + P}\left(1 - e^{-(\lambda+P)t}\right). \tag{8}$$

The cumulative extracted activity is expressed as:

$$\begin{aligned} Q(t) &= \int_0^t PA(t')\mathrm{d}t' \\ &= \frac{YP}{(\lambda + P)^2}\left[(\lambda + P)t - 1 - e^{-(\lambda+P)t}\right]. \end{aligned} \tag{9}$$

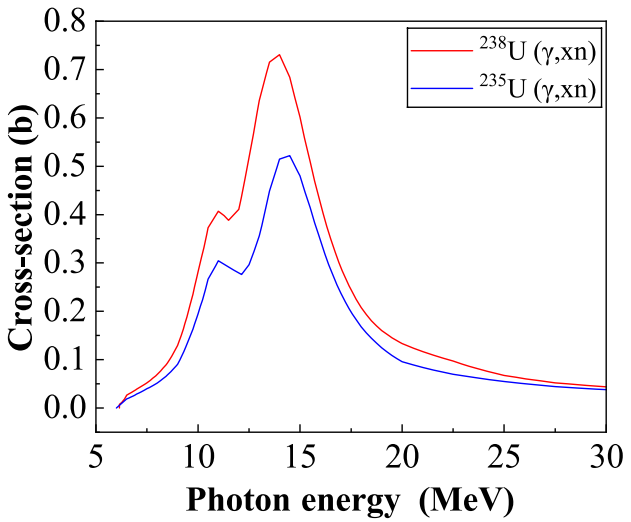

Fig. 5 (Color online) (γ, xn) reaction cross sections for ^{235}U and ^{238}U

3 Irradiation parameters analysis

The ^{99}Mo yield is primarily determined by the electron energy, beam intensity, irradiation time, molten salt composition, and dimensions. Because the per-particle yield remains constant, the total yield increases proportionally with the beam intensity. Consequently, in subsequent simulations, the beam intensity was fixed at 1 mA to focus on analyzing the impact of other parameters. In Sect. 3.1, composition analysis reveals that the LiF-UF_4 salt achieves an optimal ^{99}Mo yield (5.33×10^9 Bq) under 40 MeV electron irradiation for 1 h in a 5 cm × 6 cm × 10 cm volume. For LiF-UF_4 systems, electron energies of 40–80 MeV are most efficient. Then, Sect. 3.2 evaluates ^{99}Mo spatial distributions under 40 MeV electrons and LiF-UF_4 salt. The optimized geometry (74 cm × 74 cm × 46 cm) yielded 8.78×10^9 Bq after 1 h of irradiation. Finally, to ensure that localized boiling does not occur during the operation of the molten salt target system, the maximum temperature of the molten salt was determined. The results indicate that when the flow velocity of the molten salt is increased to 5 m/s under 80 MeV energy conditions, the maximum temperature is only 808.9 K. This effectively avoids the risk of boiling and ensures safe and stable operation of the system.

3.1 Molten salt composition and electron energy analysis

The molten salt composition is a critical factor influencing ^{99}Mo yield. Compared to enriched molybdenum targets, molten salts offer significantly lower costs, for example, base salts (e.g., LiF-BeF_2) cost 71.23 USD/kg [56], and natural uranium is approximately 200 USD/kg [57]. This cost advantage enables substantial reductions in the target fabrication costs. This section investigates ^{99}Mo yields across various molten salt compositions, with the parameters listed in Table 1. The system employs 99.95% ^{7}Li enrichment, 97% ^{37}Cl enrichment, natural uranium, and an operating temperature of 923 K.

A 40 MeV electron beam irradiated the molten salt target assembly with molten salt dimensions of 5 cm × 6 cm × 10 cm. After 1 h of irradiation, ^{99}Mo yields for various salts are presented in Table 2. LiF-UF_4 salt achieves the highest yield at 5.33×10^9 Bq, followed by NaF-UF_4 at 4.55×10^9 Bq. NaCl-$MgCl_2$-UCl_3 demonstrates the lowest yield (1.89×10^9 Bq). Notably, while the NaCl-UCl_3 salt contains the highest U-content, its ^{99}Mo yield remains comparatively low. Conversely, LiF-BeF_2-UF_4 salt, despite having the lowest U-content, achieves higher ^{99}Mo yields than both NaCl-KCl-UCl_3 and NaCl-$MgCl_2$-UCl_3 systems. Crucially, fluoride salts exhibit higher ^{99}Mo yields than chloride salts.

As shown in Table 2, ~95% of ^{99}Mo originates directly from photofission (encompassing both direct fission and decay of fission products), indicating that the bremsstrahlung photon yield governs ^{99}Mo production. For electrons, the bremsstrahlung energy loss rate satisfies [58]:

$$-\frac{\mathrm{d}E}{\mathrm{d}x} = \frac{E}{X_0}\rho, \tag{10}$$

where E denotes the electron energy, ρ represents the material density, and X_0 is the radiation length:

$$X_0 = \frac{716.4 \cdot A}{Z(Z+1)\ln(287/\sqrt{Z})}\left[\mathrm{g/cm^3}\right]. \tag{11}$$

For compounds or mixtures, the radiation length X_0 is calculated as

$$\frac{1}{X_0} = \sum_i \frac{w_i}{X_0^i}. \tag{12}$$

At an electron energy of 40 MeV, the radiation energy loss rates in different molten salts are listed in Table 2. Concurrently, bremsstrahlung photon spectra generated by 40 MeV electrons in various salts were simulated using pyPENELOPE (Fig. 6). The results revealed that the LiF-UF_4 salt exhibited the highest bremsstrahlung photon yield,

Table 1 Molten salt composition and physical properties

Molten salt	Composition (mol%)	Melting point (K)	Density (g/cm^3)	U content (mol%)
LiF-UF_4	72–28	763	4.79	9.86
LiF-BeF_2-UF_4	71.7–16–12.3	773	3.46	4.86
NaF-UF_4	72–28	896	4.22	9.86
NaCl-UCl_3	55–45	870	3.60	15.52
NaCl-KCl-UCl_3	45–25–30	810	3.08	11.54
NaCl-$MgCl_2$-UCl_3	50–33.3–16.7	778	2.50	6.26

Table 2 ^{99}Mo yields of different molten salts after 1 h of irradiation with a 40 MeV electron beam

Molten salt	^{99}Mo yield (Bq)	Photofission fraction (%)	Energy loss rate (MeV/cm)
LiF-UF_4	5.33×10^9	95.44	22.43
LiF-BeF_2-UF_4	3.31×10^9	95.23	12.72
NaF-UF_4	4.55×10^9	96.09	18.59
NaCl-UCl_3	4.14×10^9	94.95	17.05
NaCl-KCl-UCl_3	3.16×10^9	96.90	13.30
NaCl-$MgCl_2$-UCl_3	1.89×10^9	96.75	8.89

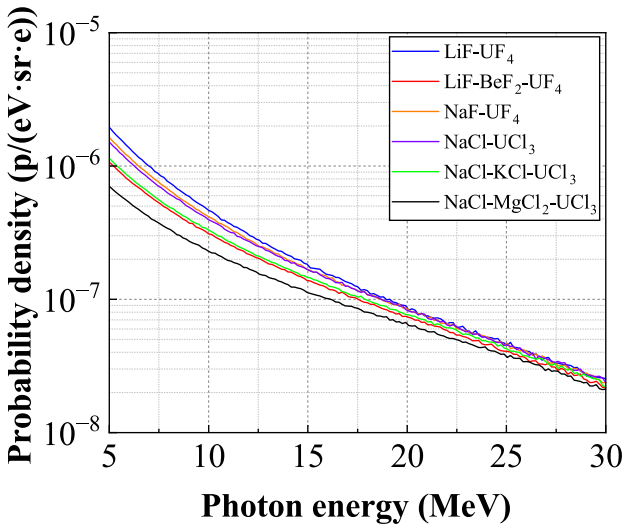

Fig. 6 (Color online) Bremsstrahlung photon energy spectra produced by 40 MeV electrons in different molten salts

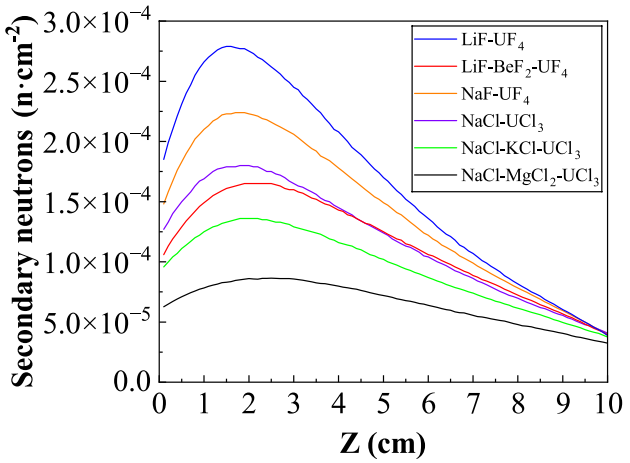

Fig. 7 (Color online) Spatial distribution of secondary neutrons from 40 MeV electrons in molten salts

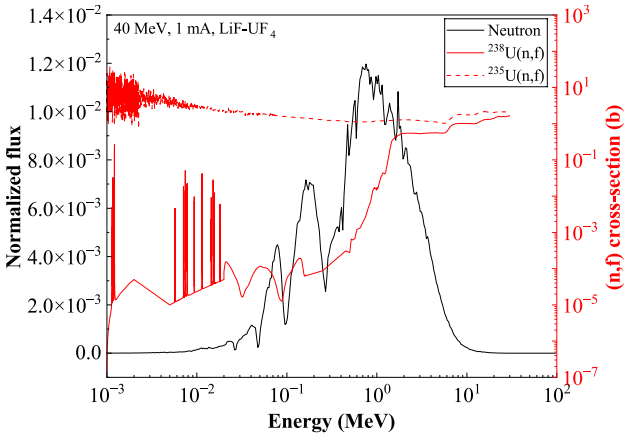

Fig. 8 (Color online) Normalized energy spectrum of secondary neutrons from 40 MeV electrons in LiF-UF_4 and ^{235,238}U(n,f) cross sections

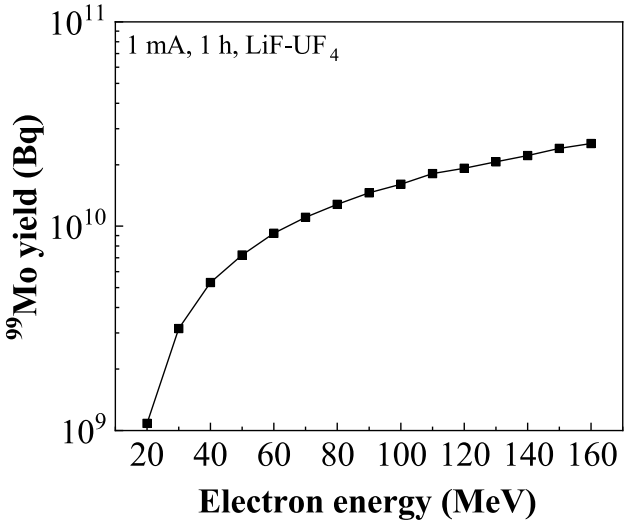

Fig. 9 ^{99}Mo yield at varying electron energies

whereas the NaCl-$MgCl_2$-UCl_3 salt exhibited the lowest. This divergence is directly correlated with the radiation energy loss rates, with LiF-UF_4 displaying the maximum radiation energy loss rate, followed by NaF-UF_4, whereas NaCl-$MgCl_2$-UCl_3 showed the minimum, thereby accounting for the superior ^{99}Mo production in the LiF-UF_4 salt.

For identical photon energies, the photonuclear reaction cross sections of uranium slightly exceed its photofission cross sections (Figs. 4 and 5), indicating that bremsstrahlung photons not only induce photofission but also generate secondary neutrons, whereas uranium fission produces additional neutrons. The spatial distributions of the secondary neutrons generated by 40 MeV electrons in various molten salts are illustrated in Fig. 7. As the penetration depth Z increases, the electron energy gradually diminishes, causing cumulative growth in the bremsstrahlung photon yield and flux, which elevates secondary neutron production. Beyond a critical depth, complete electron energy depletion coupled with photon attenuation diminishes the neutron yield. Consequently, LiF-UF_4 exhibited the highest secondary neutron yield owing to the maximal photon production. Figure 8 displays the normalized energy spectrum of secondary neutrons in LiF-UF_4, wherein fast neutrons dominate with a mean energy of ~1.23 MeV. At this energy, the neutron fission cross sections for ^{235}U and ^{238}U are low (1.21 b and 0.04 b, respectively), resulting in poor neutron utilization efficiency as most neutrons leak from the target, contributing only ~5% to the total ^{99}Mo production.

The effects of electron energy on ^{99}Mo yield in LiF-UF_4 were further investigated (Fig. 9). Photofission cross sections of uranium peak within the 5–20 MeV photon energy range. Bremsstrahlung photons exhibit a continuous spectrum: the maximum photon energy approaches the incident electron energy with low intensity, whereas the peak intensity occurs near half the electron energy [59, 60]. To optimize the photofission and photonuclear cross sections, the electron energies must exceed 40 MeV. ^{99}Mo yield increases with electron energy, though growth rates progressively diminish. However, excessively high energies generate energetic γ-rays with reduced reaction cross sections, increased shielding complexity, and undesirable side-reactions that produce radiochemical impurities. Consequently, the 40–80 MeV range balances the yield efficiency and engineering feasibility.

3.2 Molten salt dimensions and temperature analysis

With a fixed electron beam spot size (e.g., 1 cm), the molten salt target dimensions critically impact ^{99}Mo yield. Undersized targets underutilize the beam flux, whereas oversized targets increase salt consumption and costs. FLUKA simulations revealed ^{99}Mo spatial distributions via residual nuclei calculations under 40 MeV, 1 mA electron irradiation for 1 h (Fig. 10). The electron beam propagates along the positive *Z*-direction, perpendicular to the *XY*-plane. In the *XY*-plane, the residual nuclei exhibited a concentric distribution from the beam point, with the density decreasing radially. Along the *XZ*-plane, the residual nuclei diminish exponentially along *Z*, becoming negligible beyond 90 cm. Statistical analysis confirmed that 98% of the residual nuclei were concentrated within ±37 cm (*X*/*Y*) and 46 cm (*Z*). Thus, the optimal dimensions of 74 cm × 74 cm × 46 cm achieved a peak yield of 8.78×10^9 Bq.

For accelerator targets, a core challenge is the effectively removal of the substantial heat generated by beam energy deposition to prevent local overheating of the target [61, 62]. To evaluate the temperature distribution of a molten salt target (LiF-UF_4, 74 cm × 74 cm × 46 cm), the three-dimensional energy deposition distribution of an electron beam (40/80 MeV, 1 mA) in the target was calculated using FLUKA. The energy deposition data were imported into ANSYS Fluent for thermal-hydraulic calculations to obtain a steady-state temperature field. During actual operation, beam energy deposition can form hot spots in local areas, posing a risk of molten salt boiling, thus making efficient heat removal critical. However, owing to the large volume of the molten salt target, the heat deposited by the beam is insufficient to maintain the entire region in a molten state, necessitating additional heating devices to prevent

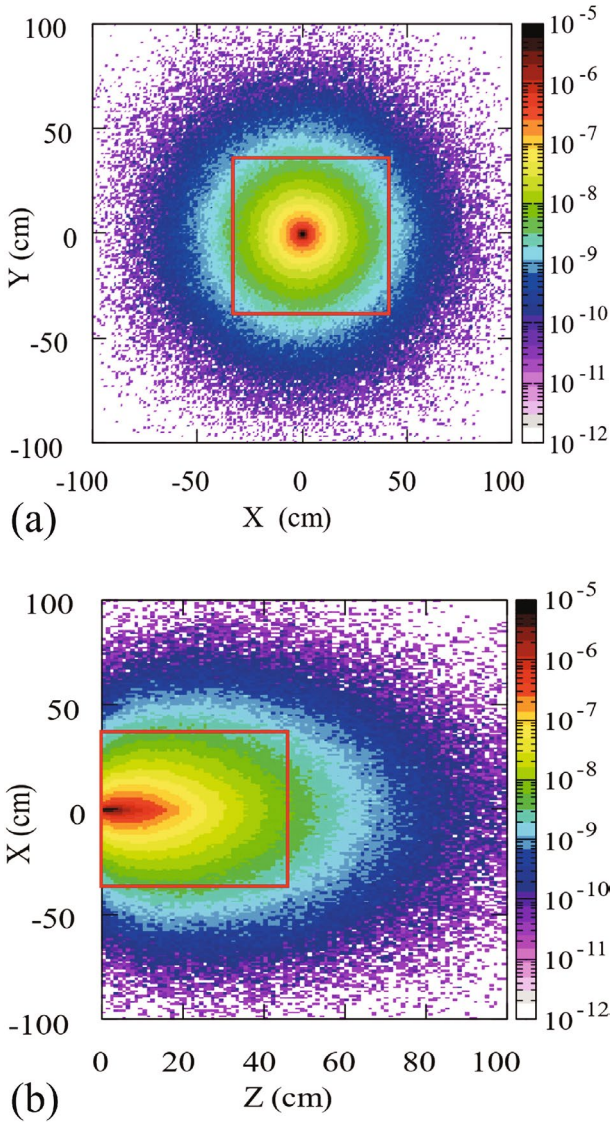

Fig. 10 (Color online) Spatial distribution of residual nuclei: **a** *XY*-plane, **b** *XZ*-plane

solidification. To simplify the computational model, a constant temperature boundary condition of 773 K was applied to the molten salt region in Fluent.

Figure 11 shows the steady-state temperature distribution at $Z = 0.2$ cm under 40 MeV and 80 MeV electron beam irradiation. The electron beam is incident vertically with a beam spot radius of only 1 cm, and owing to the short electron range, energy is primarily deposited near the injection point, forming a local hot spot. The maximum temperature point was located at approximately ($X = 0$ cm, $Y = 0$ cm, $Z = 0.2$ cm). The molten salt flowed upward (inlet at the bottom and outlet at the top) and continuously removed heat from the vicinity of the hot spot, resulting in a temperature gradient band along the flow direction. The variation in the maximum temperature within the molten salt target with the

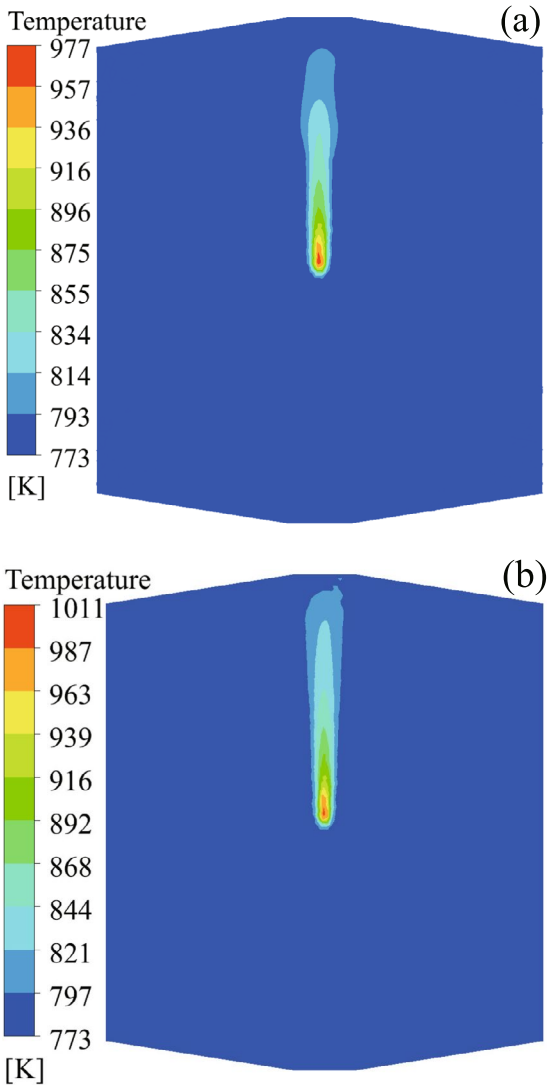

Fig. 11 (Color online) The steady-state distribution at $Z = 0.2$ cm within the molten salt target: **a** $E_e = 40$ MeV, and **b** $E_e = 80$ MeV

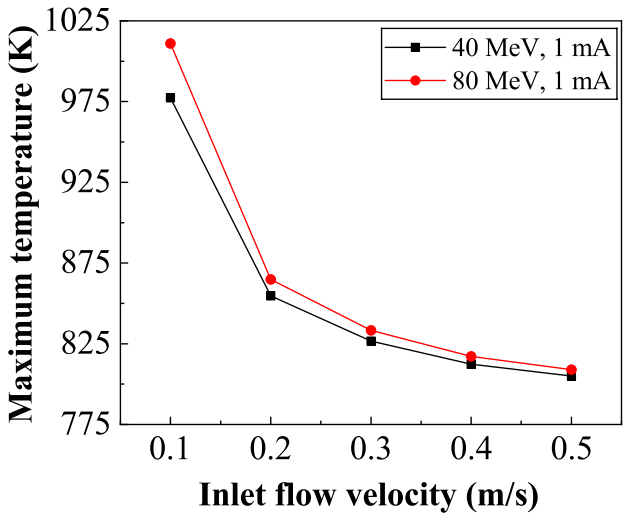

Fig. 12 (Color online) Variation of the maximum temperature in the molten salt with the inlet flow velocity

inlet flow velocity is shown in Fig. 12. As the flow velocity increased from 0.1 to 0.5 m/s, the maximum temperature decreased from 977.3 to 805.0 K (40 MeV) and from 1011.0 to 808.9 K (80 MeV). At the same flow velocity, the 80 MeV beam induced a higher maximum temperature than the 40 MeV beam; however, this temperature difference gradually diminished as the flow velocity increased. Importantly, all maximum temperatures remained well below the boiling point (above 1773 K [63]), indicating that the temperature distribution remained within a safe range. The heat dissipation performance of the flowing molten salt target is significantly superior to that of solid targets, which is attributed to their distinct thermal-hydraulic mechanisms. Solid targets primarily rely on molecular thermal vibrations for heat conduction, which is a single and less efficient heat transfer pathway. In contrast, a flowing molten salt target incorporates an additional forced convection mechanism on this basis, significantly enhancing heat transfer through convective heat exchange. The continuous flow of molten salt efficiently carries away heat, thereby preventing local overheating and ensuring more stable and efficient heat transport [64, 65]. This allows the molten salt target to meet heat dissipation requirements through its flow, eliminating the need for additional cooling devices, simplifying the system structure, and reducing costs.

4 Online extraction computational analysis

Current accelerator-based ^{99}Mo production predominantly employs solid targets (e.g., metallic molybdenum, molybdenum oxide, uranium oxide). Solid target fabrication involves homogenizing powders (synthesized via dissolution-oxidation processes) with a carrier matrix, followed by mechanical compaction of the mixture. Isotope extraction requires multiple steps: target disassembly, sectioning, dissolution, wet or dry separation, and purification, yielding a complex workflow [5]. Therefore, leveraging ^{99}Mo's existence as insoluble particles in molten salt and the fluid properties of liquid molten salts, this study adopted a bubbling method for ^{99}Mo online extraction analysis.

Based on the optimization results in Sect. 3, a configuration with a 40 MeV electron energy, LiF-UF_4 molten salt (74 cm × 74 cm × 46 cm) was selected. Figure 13 illustrates the variation of ^{99}Mo yield with irradiation time. The ^{99}Mo yield increased progressively with the irradiation time, whereas the amount of decay also increased. Consequently, production and decay eventually reached equilibrium,

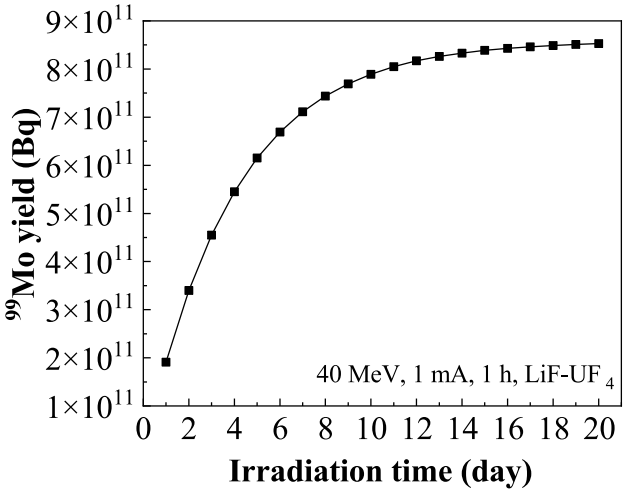

Fig. 13 ^{99}Mo yield variation with irradiation time

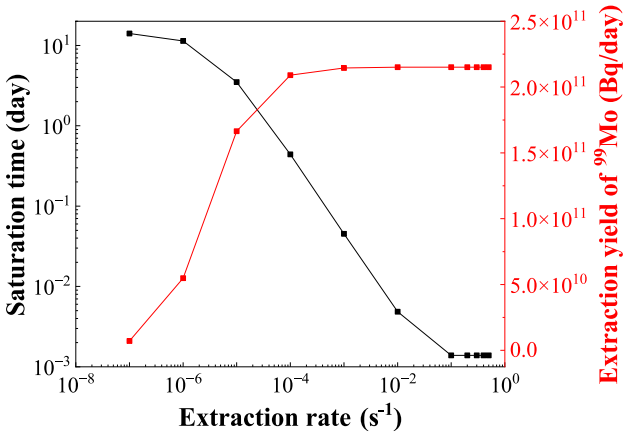

Fig. 15 (Color online) Equilibrium time and saturated extraction quantity at different extraction efficiencies

saturating the yield at 8.53×10^{11} Bq. Utilizing this saturated yield and Eq. (6), the ^{99}Mo production rate Y under these conditions is calculated as 2.49×10^{6} Bq/s.

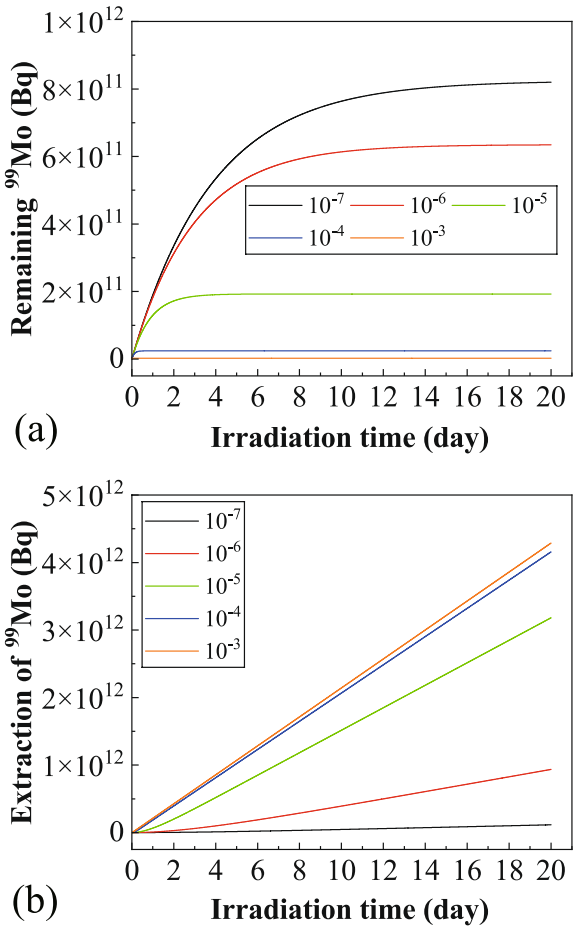

Fig. 14 (Color online) Variation of ^{99}Mo activity in molten salt **a** and cumulative extraction quantity **b** over time under different extraction efficiencies

Figures 14 and 15 display the residual ^{99}Mo activity in molten salts, cumulative extraction quantity, equilibrium time, and saturated extraction yields at different extraction efficiencies. Higher extraction efficiencies reduce residual ^{99}Mo activity, accelerate equilibrium attainment, and lower the equilibrium activity levels. At an extraction efficiency of 10^{-3} s^{-1}, equilibrium was achieved in ~65 min. Once the ^{99}Mo activity in the molten salt saturates, the extraction quantity per unit time also stabilizes, resulting in a linear increase in the cumulative yield. Saturated extraction yield initially increases with extraction efficiency and stabilizes: at 10^{-4} s^{-1}, it stabilizes at 2.09×10^{11} Bq/day; at 10^{-3} s^{-1}, it increases to 2.15×10^{11} Bq/day. Balancing equilibrium time against saturated yield, the optimal extraction efficiency was determined to be 10^{-4} s^{-1} with an equilibrium time of 10.57 h and a saturated yield of 2.09×10^{11} Bq/day.

5 ^{99}Mo production estimation and comparison with China's demand

The stable daily production of ^{99}Mo via electron accelerator irradiation of molten salts can support domestic demand. The proposed technology enables continuous operation through the flexibility of electron accelerators and the online extraction capabilities of molten salt targets. Furthermore, through systematic optimization of electron energy, target parameters, and temperature control, efficient supply demand matching and autonomous security for China's ^{99}Mo supply chain can be achieved.

Using optimized parameters from Sect. 3 and Sect. 4 (40/80 MeV electrons, 1 mA beam intensity, LiF-UF$_4$

molten salt (74 cm × 74 cm × 46 cm), 923 K salt temperature, 10^{-4} s^{-1} extraction efficiency), annual ^{99}Mo extraction yields were calculated. Under these conditions, the ^{99}Mo production rates reached 2.49×10^{6} Bq/s (40 MeV) and 6.35×10^{6} Bq/s (80 MeV). Accounting for cyclic accelerator maintenance (3 days of irradiation + 0.5 days of maintenance cycles), Fig. 16 illustrates the annual ^{99}Mo activity and cumulative extraction dynamics. Each cycle features rising ^{99}Mo activity during irradiation and decays rapidly during maintenance, with cumulative extraction increasing quasi-linearly. The annual yields differed significantly: 6.53×10^{13} Bq (1764.86 Ci) at 40 MeV versus 1.66×10^{14} Bq (4486.49 Ci) at 80 MeV.

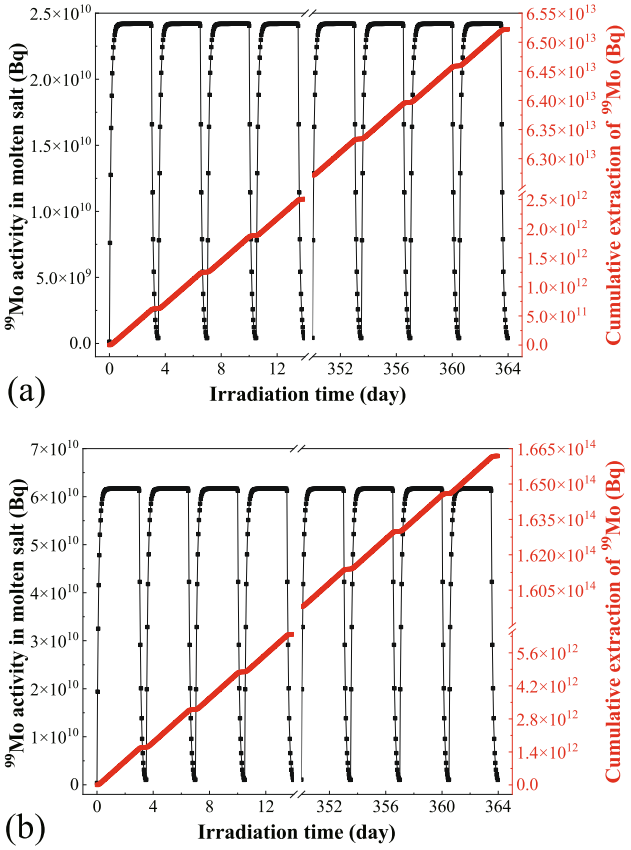

Fig. 16 (Color online) Annual dynamics of ^{99}Mo activity in molten salt and cumulative extraction quantity: **a** E_e = 40 MeV, and **b** E_e = 80 MeV

As shown in Table 3, compared with other ^{99}Mo production methods proposed by researchers, this study shows no significant advantage in yield, only exceeding the result reported by Villa et al. [66]. However, this study employs natural uranium as the raw material, which offers higher safety and easier availability than schemes requiring LEU. Furthermore, studies by Minato et al. [67], Gao et al. [32], Villa et al. [66], and Bondar et al. [68] all utilize highly enriched molybdenum targets and highly enriched zirconium targets, which entail high costs and complex production processes. Therefore, the notable advantages of this study in terms of safety, flexibility, and online production capability are sufficient to compensate for the lower yield.

In clinical practice, the administered activity of ^{99m}Tc varies with specific radiopharmaceuticals, disease types, and patient conditions. For instance, ^{99m}Tc-MDP (Technetium-99m methylene diphosphonate) employed in bone scintigraphy requires a single administered dose of 740–1110 MBq (20–30 mCi) of ^{99m}Tc, which necessitates 34–51 mCi of ^{99}Mo [69–71]. In contrast, ^{99m}Tc-DMSA (Technetium-99m dimercaptosuccinic acid) for renal imaging requires 11.1–111 MBq (0.3–3 mCi) of ^{99m}Tc, corresponding to a ^{99}Mo requirement of 0.5–5 mCi [72]. Excluding other losses, based on the maximum (51 mCi) and minimum (0.5 mCi) ^{99}Mo requirements per dose, a 40 MeV facility can supply approximately 34,605 (high-dose scenario) to 3,529,720 (low-dose scenario) patient doses annually, while an 80 MeV facility can provide approximately 87,970 (high-dose

Table 3 Comparison of different production methods for ^{99}Mo

Researcher	Device type	Beam conditions	Target material	Primary reaction	^{99}Mo yield	Refs.
Han et al	Subcritical blanket system	D-D neutron 1×10^{14} n/s	LEU, ^{235}U@19.75%	^{235}U(n,f)	157 Ci/day	[9]
Villa et al	R-7 cyclotron	27 MeV	^{96}Zr @100%	^{96}Zr(α,n)	1.62 MBq/(μA·h)	[66]
Minato et al	Deuteron accelerator	40 MeV, 2 mA	$^{100}MoO_3$ (^{100}Mo@95.90%)	^{100}Mo(n,2n)	17.84 Ci/day	[67]
Gao et al	Electron accelerator	50 MeV, 1 mA	Enriched molybdenum (^{100}Mo@99.813%)	^{100}Mo(γ,n)	33 Ci/day	[32]
Bondar et al	Medical cyclotron Eclipse RD	11 MeV	Enriched molybdenum (^{100}Mo@92.2%)	^{100}Mo(p,2n)	30.9 MBq/(μA·h)	[68]
This work	Electron accelerator	40–80 MeV, 1mA	LiF-UF_4@natural U	^{238}U(γ,f)	1764.86 Ci/year@40 MeV 4486.49 Ci/year@80 MeV	

scenario) to 8,972,980 (low-dose scenario) patient doses per year. Furthermore, projections from China's "Medium-to-Long-Term Development Plan for Medical Isotopes (2021–2035)" indicate that the national ^{99}Mo demand in 2030 will reach 2.74×10^4 Ci. A single 40 MeV accelerator and an 80 MeV unit could satisfy 6.44% and 16.37% of the national demand, respectively. An increase in beam intensity can further reduce the number of facilities required.

To minimize decay losses during transportation and leverage the deployment flexibility and inherent safety advantages of accelerator systems, deploying ^{99}Mo production facilities in major cities (e.g., Beijing, Shanghai, Shenzhen, Chengdu, and Wuhan) is recommended. Integrated with existing ^{18}F distribution networks, this strategy would achieve rapid nationwide ^{99}Mo supply delivery, covering 95% of the population within the effective distribution radius [73].

6 Conclusion

This study proposes an approach for ^{99}Mo production via electron accelerator irradiation of natural-uranium-bearing liquid molten salts, primarily exploiting the ^{238}U(γ,f) reaction pathway. The key advantages of this approach include low nuclear proliferation risk, online extraction capability, and reduced target fabrication costs. Through a systematic feasibility analysis and parameter optimization, the following principal conclusions were drawn:

1. Fluoride–based systems exhibit higher ^{99}Mo yields than chloride-based systems due to their higher bremsstrahlung energy deposition rates and photon production.
2. Following comprehensive assessment of yield efficiency, shielding costs, and technical feasibility, an electron energy range of 40–80 MeV is identified as optimal.
3. As the inlet molten salt flow velocity increases, the maximum temperature inside the molten salt target gradually decreases. At a flow velocity of 0.5 m/s and an energy of 80 MeV, the maximum system temperature is only 808.9 K, which is significantly lower than the boiling point of 1773 K, ensuring a safe operational state.
4. The online extraction capability of liquid molten salt targets significantly improves production flexibility. By balancing the equilibrium time and saturated yield, the optimal extraction efficiency was 10^{-4} s^{-1}.
5. The maximum annual production capacity of ^{99}Mo reaches 4486.49 Ci with 80 MeV, which is sufficient to meet millions of diagnostic procedures and accounts for approximately 16.37% of China's projected total demand for 2030.

This study establishes an innovative technical pathway for ^{99}Mo production, although it primarily focuses on feasibility analysis and partial critical parameters. Several limitations require further refinement, such as the cladding alloy thickness and molten salt target configuration. The 0.5 cm thick nickel alloy cladding adopted in this study necessitated a rigorous evaluation of its impact on electron beam attenuation. Concurrently, the tentatively proposed cuboid molten salt target configuration warrants a comparative assessment against alternative geometries (e.g., spherical and cylindrical geometries). Future work must integrate shielding design, thermal-hydraulic analysis, and insulation system optimization to achieve systematic structural refinement of molten salt targets. Additionally, the bubbling online extraction system requires an in-depth investigation of the physicochemical properties of ^{99}Mo in molten salts. These advancements will establish a more robust foundation for the industrial-scale application of this methodology.

Author contributions All authors contributed to the study conception and design. Material preparation, data collection and analysis were performed by Jun-Ze Lin, Bo-Lin Fu, De-Yang Cui, Xiao-Xiao Li, Cheng-Gang Yu, Jian-Hui Wu, Jin-Gen Chen, Xiang-Zhou Cai. The first draft of the manuscript was written by Jun-Ze Lin, and all authors commented on the previous versions of the manuscript. All authors read and approved the final manuscript.

Data availability The data that support the findings of this study are openly available in Science Data Bank at https://cstr.cn/31253.11.sciencedb.j00186.00885 and https://doi.org/10.57760/sciencedb.j00186.00885.

Declarations

Conflict of interest Xiang-Zhou Cai is an editorial board member for Nuclear Science and Techniques and was not involved in the editorial review, or the decision to publish this article. All authors declare that there are no conflict of interest.

References

1. M.A.B. Naafs, The global impact of the Mo-99 shortage. Biomed. J. Sci. Tech. Res. **4**, 1–6 (2018). https://doi.org/10.2671/BJSTR.2018.04.001114
2. Z.F. Luo, Y.X. Wu, J.X. Liang, Methods for production of medical radioisotope ^{99}Mo. J. Isot. **31**, 129–142 (2018). https://doi.org/10.7538/tws.2018.31.03.0129
3. V. Hanemaayer, F. Benard, K.R. Buckley et al., Solid targets for ^{99m}Tc production on medical cyclotrons. J. Radioanal. Nucl. Chem. **299**, 1007–1011 (2014). https://doi.org/10.1007/s10967-013-2626-4
4. Nuclear Energy Agency, *The supply of medical radioisotopes: 2017 medical isotope supply review:*^{99}Mo/^{99m}T *market demand and production capacity projection 2017–2022* (OECD Publishing, Paris, 2017)
5. Y. He, F. Liu, R. Zhang, Production techniques of fission molybdenum-99 via highly enriched uranium: a review. J. Isot. **31**, 157–164 (2018). https://doi.org/10.7538/tws.2018.31.03.0157
6. Z.W. Li, Y.C. Han, X.Y. Wang et al., Production status and technical prospects of medical radioisotope ^{99}Mo/^{99m}T. Nucl. Phys. Rev. **36**, 170–183 (2019). https://doi.org/10.11804/NuclPhysRev.36.02.170

7. M. Ahmad, G. Vandegrift, P. Cristini, Molybdenum-99 (^{99}Mo): past, present, and future. Sci. Technol. Nucl. Install. **2014**, 839369 (2014). https://doi.org/10.1155/2014/839369
8. R. Raposio, G. Thorogood, K. Czerwinski et al., Development of LEU-based targets for radiopharmaceutical manufacturing: a review. Appl. Radiat. Isot. **148**, 225–231 (2019). https://doi.org/10.1016/j.apradiso.2019.03.019
9. H.H. Xiong, Q.S. Zeng, Y.C. Han et al., Neutronics analysis of a subcritical blanket system driven by a gas dynamic trap-based fusion neutron source for ^{99}Mo production. Nucl. Sci. Tech. **34**, 49 (2023). https://doi.org/10.1007/s41365-023-01206-2
10. R.V. Noorden, Radioisotopes: the medical testing crisis. Nature **504**, 202–204 (2013). https://doi.org/10.1038/504202a
11. L. Stefanini, F.H.E. de Haan-de Wilde, High flux reactor continued safe operation: time limited ageing analyses. In *ASME 2020 Pressure Vessels and Piping Conference–Volume 8: Operations, Applications, and Components,* Virtual, Online, 3 August 2020, V008T08A010. https://doi.org/10.1115/PVP2020-21032
12. High Flux Reactor at Petten temporarily shut down. (Authority for Nuclear Safety and Radiation Protection, 2024). https://english.autoriteitnvs.nl/latest/news/2024/10/22/high--flux--reactor--at--petten--temporarily--shut--down
13. S.V. Dyck, The BR2 reactor: short history, characteristics and utilization. In *Encyclopedia of Nuclear Energy,* 2021, pp. 96–104. https://doi.org/10.1016/B978-0-12-819725-7.00078-7
14. Cabinet approval for new South African research reactor. (World Nuclear News, World Nuclear Association, 2021) https://www.world-nuclear-news.org/Articles/Cabinet-approval-for-new-South-African-research-re
15. M.V. Huisman, Medical Isotope Production Reactor design for a small sized aqueous homogeneous reactor for producing molybdenum-99 for regional demand. Master Thesis, Delft University of Technology (2013)
16. R.M. Ball, *Testimony before the congressional committee on US resources on the production of Mo-99 with aqueous homogeneous reactors* (Mike Synar, Chairman, 1992)
17. Q.M. Deng, M.Q. Li, Z.Y. Cheng, Application of ^{99}Mo production through medical isotope production reactor (MIPR). Chin. J. Nucl. Sci. Eng. **26**, 165–167 (2006)
18. X.M. Song, W.H. Niu, Optimization of 200 kW medical isotope production reactor design. In *Homogeneous aqueous solution nuclear reactors for the production of Mo-99 and other shortlived radioisotopes,* 2008, p.17
19. Q.M. Deng, Z.Y. Chen, M.L. Li et al., Feasibility research of ^{99}Mo, ^{131}I and ^{89}Sr production by medical isotope production reactor. Nucl. Power Eng. **32**, 115–118 (2011)
20. Y. Zhao, X.H. Liu, Y.L. Zhang et al., Emergency reactor trip system design of MIPR. J. Isot. **32**, 128–132 (2019). https://doi.org/10.7538/tws.2018.youxian.037
21. H.X. Li, Z.D. Xia, F. Liu et al., Conceptual design of accelerator driven subcritical aqueous homogeneous reactor for isotope production. At. Energy Sci. Technol. **58**, 393–400 (2023). https://doi.org/10.7538/yzk.2023.youxian.0254
22. X.Z. Kang, Study of noble-metal fission nuclide ^{99}Mo generation and migration in thorium based Molten Salt Reactor. Doctoral Thesis, University of Chinese Academy of Sciences (2021). https://doi.org/10.27585/d.cnki.gkshs.2021.000024
23. L. Chen, R. Yan, X.Z. Kang et al., Study on the production characteristics of ^{131}I and ^{90}Sr isotopes in a molten salt reactor. Nucl. Sci. Tech. **32**, 33 (2021). https://doi.org/10.1007/s41365-021-00867-1
24. J. Moon, K. Myhre, H. Andrews et al., Molybdenum-99 from molten salt reactor as a source of technetium-99m for nuclear medicine: past, current, and future of molybdenum-99. Nucl. Technol. **209**, 787–808 (2023). https://doi.org/10.1080/00295450.2022.2158666
25. G.Y. Zheng, H.L. Wu, J.P. Wang et al., Thorium-based molten salt SMR as the nuclear technology pathway from a market-oriented perspective. Ann. Nucl. Energy **116**, 177–186 (2018). https://doi.org/10.1016/j.anucene.2018.02.004
26. A.L. Tataurov, O.S. Feinberg, Molten Salt Reactor for ^{99}Mo production. At Energy **122**, 299–303 (2017). https://doi.org/10.1007/s10512-017-0270-8
27. D.Y. Chuvilin, V.A. Zagryadskii, New method of producing ^{99}Mo in molten-salt fluoride fuel. At Energy **107**, 185–193 (2009). https://doi.org/10.1007/s10512-010-9214-2
28. M.N. Stoddard, J.N. Harb, M.J. Memmott, Numerical analysis of isotope production in molten salt reactors: a case study for Molybdenum-99 production. Ann. Nucl. Energy **129**, 56–61 (2019). https://doi.org/10.1016/j.anucene.2019.01.021
29. Y. Wang, Z.F. Guo, L. Wang et al., Development status and prospect for the medical isotope molybdenum-99 produced by electron accelerator. J. Isot. **35**, 114–127 (2022). https://doi.org/10.7538/tws.2022.35.02.0114
30. G. Pupillo, J. Esposito, F. Haddad et al., Accelerator-based production of ^{99}Mo: a comparison between the ^{100}Mo(p, x) and ^{96}Zr(α, n) reactions. J. Radioanal. Nucl. Chem. **305**, 73–78 (2015). https://doi.org/10.1007/s10967-015-4091-8
31. S. Sekimoto, K. Tatenuma, Y. Suzuki et al., Separation and purification of ^{99m}Tc from ^{99}Mo produced by electron linear accelerator. J. Radioanal. Nucl. Chem. **311**, 1361–1366 (2017). https://doi.org/10.1007/s10967-016-4959-2
32. X. Gao, P. Zhang, J. Li et al., Production of ^{99}Mo via photoneutron reaction using a 50 MeV electron linear accelerator. J. Radioanal. Nucl. Chem. **332**, 3037–3045 (2023). https://doi.org/10.1007/s10967-023-09003-2
33. A. Celler, X. Hou, F. Bénard et al., Theoretical modeling of yields for proton-induced reactions on natural and enriched molybdenum targets. Phys. Med. Biol. **56**, 5469 (2011). https://doi.org/10.1088/0031-9155/56/17/002
34. D.S. Chen, Q.G. Huang, S.W. Cao et al., Comparative experiment on the preparation of ^{99}Mo/^{99m}T via electron and proton irradiation of ^{100}Mo. J. Isot. **38**, 30–38 (2024). https://doi.org/10.7538/tws.2024.youxian.081
35. J. Chen, M.T. Fu, Y.Y. Yao et al., Research progress in adsorption and separation of medical isotope ^{99}Mo. J. Isot. **38**, 173–184 (2023). https://doi.org/10.7538/tws.2023.youxian.040
36. R. Yang, J.X. Shu, X. Luo, Research progress on low specific activity ^{99}Mo-^{99m}T generators. J. Isot. **38**, 48–55 (2025). https://doi.org/10.7538/tws.2024.youxian.113
37. P. Tkac, G.F. Vandegrift, Recycle of enriched Mo targets for economic production of ^{99}Mo/^{99m}T medical isotope without use of enriched uranium. J. Radioanal. Nucl. Chem. **308**, 205–212 (2016). https://doi.org/10.1007/s10967-015-4357-1
38. M. Kawabata, S. Motoishi, H. Saeki et al., Recovery efficiency of enriched ^{100}MoO3 irradiated by accelerator neutrons. J. Phys. Soc. Jpn. **86**, 053201 (2017). https://doi.org/10.7566/JPSJ.86.053201
39. G.R. Piefer, K.M. Pitas, E.N. Van et al., Mo-99 production using a subcritical assembly. In *Proceedings of the 1st Annual Mo–99 Topical Meeting,* Santa Fe, New Mexico, 4–7 December 2011
40. L. Ren, Y.C. Han, J.C. Zhang et al., Neutronics analysis of a stacked structure for a subcritical system with LEU solution driven by a D-T neutron source for ^{99}Mo production. Nucl. Sci. Tech. **32**, 123 (2021). https://doi.org/10.1007/s41365-021-00968-x
41. L. Ren, Z.W. Li, Y.C. Han et al., Neutronics study of a subcritical system driven by external neutron source for ^{99}Mo production. Fusion Eng. Des. **165**, 112263 (2021). https://doi.org/10.1016/j.fusengdes.2021.112263

42. M. Hagiwara, H. Yashima, T. Sanami et al., Measurement of the excitation function of ^{96}Zr(α, n) for an alternative production source of medical radioisotopes. J. Radioanal. Nucl. Chem. **318**, 569–573 (2018). https://doi.org/10.1007/s10967-018-6118-4
43. T. Ruth, Accelerating production of medical isotopes. Nature **457**, 536–537 (2009). https://doi.org/10.1038/457536a
44. H. Naik, S.V. Suryanarayana, K.C. Jagadeesan et al., An alternative route for the preparation of the medical isotope ^{99}Mo from the ^{238}U(γ,f) and ^{100}Mo(γ,n) reactions. J. Radioanal. Nucl. Chem. **295**, 807–816 (2013). https://doi.org/10.1007/s10967-012-1958-9
45. H. Naik, V.T. Nimje, D. Raj et al., Mass distribution in the bremsstrahlung-induced fission of ^{232}Th, ^{238}U and ^{240}Pu. Nucl. Phys. A **853**, 1–25 (2011). https://doi.org/10.1016/j.nuclphysa.2011.01.009
46. H. Thierens, D.D. Frenne, E. Jacobs et al., Product yields for the photofission of ^{235}U and ^{238}U with 25-MeV bremsstrahlung. Phys. Rev. C **14**, 1058 (1976). https://doi.org/10.1103/PhysRevC.14.1058
47. R.A. Schmitt, N. Sugarman, Uranium photofission yields. Phys. Rev. **95**, 1260 (1954). https://doi.org/10.1103/PhysRev.95.1260
48. M.R. William, Fission product yield evaluation. Doctorates Thesis, University of Birmingham (1995)
49. R. Han, Z.Q. Chen, G.Y. Tian et al., Study of medical radioisotopes production by accelerator induced reactions with FLUKA. Nucl. Phys. Rev. **37**, 913–917 (2020). https://doi.org/10.11804/NuclPhysRev.37.2020025
50. B. Jiang, B.B. Tian, H.T. Jing et al., Feasibility of medical radioisotope production based on the proton beams at China Spallation Neutron Source. Nucl. Sci. Tech. **35**, 102 (2024). https://doi.org/10.1007/s41365-024-01438-w
51. T. Amin, A. Infantino, R. Barlow et al., Validating production of PET radionuclides in solid and liquid targets: comparing Geant4 predictions with FLUKA and measurements. Appl. Radiat. Isot. **133**, 61–67 (2018). https://doi.org/10.1016/j.apradiso.2017.12.009
52. P. Adamson, C. Cannon, S. Williams, Bremsstrahlung produced by 5 keV electrons incident on BeO and NaCl. Nucl. Instrum. Meth. B **490**, 43–47 (2021). https://doi.org/10.1016/j.nimb.2021.01.006
53. X. Xue, X. Liu, C.X. Chen et al., Thermal and thermodynamic performance simulation and evaluation of large molten salt storage tanks and foundations. Appl. Therm. Eng. **273**, 126967 (2025). https://doi.org/10.1016/j.applthermaleng.2025.126967
54. Evaluated Nuclear Data File (2025) https://www-nds.iaea.org/exfor/endf.htm
55. L.Y. He, G.C. Li, S.P. Xia et al., Effect of ^{37}Cl enrichment on neutrons in a molten chloride salt fast reactor. Nucl. Sci. Tech. **31**, 27 (2020). https://doi.org/10.1007/s41365-020-0740-x
56. D.F. Williams, K.T. Clarno, Evaluation of salt coolants for reactor applications. Nucl. Technol. **163**, 330–343 (2017). https://doi.org/10.13182/NT08-A3992
57. CNEA International Natural Uranium Price Forecast Index (2024) https://news.bjx.com.cn/html/20240716/1389308.shtml
58. X.L. Wang, C. Li, M. Shao et al., *Particle detection technology* (University of Science and Technology of China Press, Hefei, 2009)
59. M.J. Berger, S.M. Seltzer, Bremsstrahlung and photoneutrons from thick tungsten and tantalum targets. Phys. Rev. C **2**, 621 (1970). https://doi.org/10.1103/PhysRevC.2.621
60. D. Tan, B. Heaton, Bremsstrahlung intensity and spectrum-theoretical deduction and discussion. Appl. Radiat. Isot. **45**, 1101–111 (1994). https://doi.org/10.1016/0969-8043(94)90190-2
61. W.J. Cui, Z.Y. He, Q. Zhao et al., Temperature control for spallation target in accelerator driven system. Nucl. Instrum. Meth. B **448**, 5–10 (2019). https://doi.org/10.1016/j.nimb.2019.03.059
62. H.C. Yang, X.F. Yang, Y.H. Tang et al., Design of high-energy X-ray conversion target based on linear electron accelerator. Appl. Radiat. Isot. **224**, 111951 (2025). https://doi.org/10.1016/j.apradiso.2025.111951
63. A.M. Perry, A high-yield molten-salt burst reactor. No. CONF–690102. Oak Ridge National Lab (1970)
64. G.L. Yoder, Examination of liquid fluoride salt heat transfer. In *International Congress on Advances in Nuclear Power Plants,* North Carolina, United States of America, 6–9 April 2014, p.14332
65. Y.S. Chen, J. Tian, S.D. Sun et al., Characteristics of the laminar convective heat transfer of molten salt in concentric tube. Appl. Therm. Eng. **125**, 995–1001 (2017). https://doi.org/10.1016/j.applthermaleng.2017.07.043
66. N.E. Villa, V.S. Skuridin, V.M. Golovkov et al., Cyclotron production of ^{99}Mo radionuclide by bombarding zirconium targets with alpha particle beams. Russ. Phys. J. **62**, 605–609 (2019). https://doi.org/10.1007/s11182-019-01753-5
67. F. Minato, K. Tsukada, N. Sato et al., Measurement and estimation of the ^{99}Mo production yield by ^{100}Mo(n,2n)^{99}Mo. J. Phys. Soc. Jpn. **86**, 114803 (2017). https://doi.org/10.7566/JPSJ.86.114803
68. B.M. Bondar, B.Y. Leshchenko, I.M. Kadenko et al., Determination of the experimental yield of ^{99m}Tc in (p,2n) nuclear reaction on enriched ^{100}Mo sample with application of 11-MeV medical cyclotron. Appl. Radiat. Isot. **189**, 110431 (2022). https://doi.org/10.1016/j.apradiso.2022.110431
69. J. He, Y.P. Zhong, S. Zhang, Technetium-99m-methylene diphosphonate single photon emission computed tomography/computed tomography combined with prostate-specific antigen/free prostate-specific antigen ratio for bone metastasis of prostate cancer. World J. Clin. Cases. **12**, 4082–4090 (2024). https://doi.org/10.12998/wjcc.v12.i20.4082
70. M. Srivastava, R. Pagala, V. Kendarla et al., Technetium-99m methylene diphosphonate bone scan in evaluation of insufficiency fractures-A pictorial assay and experience from South India. World J. Nucl. Med. **20**, 355–360 (2021). https://doi.org/10.4103/wjnm.wjnm_155_20
71. R. Gupta, S. Garg, T.F. Heston, Mo99-Tc99m generator. StatPearls [Internet]. StatPearls Publishing (2023)
72. R. Lim, N. Kwatra, V.F. Valencia et al., Review of the clinical and technical aspects of ^{99m}Tc-dimercaptosuccinic acid renal imaging: The comeback "Kit''. J. Nucl. Med. Tech. **52**, 199–204 (2024). https://doi.org/10.2967/jnmt.123.267185
73. W.D. Yang, F. Kang, Y. Chen et al., Landscape of nuclear medicine in China and its progress on theranostics. J. Nucl. Med. **65**, 29S-37S (2024). https://doi.org/10.2967/jnumed.123.266968